PFC/JA-87-36

Three-dimensional Equilibria in DRAKONs

Y. T. Lau

October 1987

Plasma Fusion Center
Massachusetts Institue of Technology
Cambridge, MA 02139 USA

This work was supported by the U. S. Department of Energy Contract No. DE-AC02-78ET51013. Reproduction, translation, publication, use and disposal, in whole or in part, by or for the United States government is permitted.

Submitted for publication in : Nuclear Fusion

Three-dimensional equilibria in DRAKONs

Y. T. Lau

Plasma Fusion Center

Massachusetts Institute of Technology

Cambridge, MA 02139

October 1987

An analytic formula of the second-order equilibrium beta limit for triangular-CREL DRAKONs with arbitrary pressure profile is derived. Its predictions for a parabolic pressure profile are compared with the full third-order numerical results, leading to a semi-analytic formula. The beta limits obtained here are much lower than those obtained previously; for example, for a DRAKON with straight sections and CRELs equal in length and with triangular CRELs of aspect ratio 2, the peak beta limit is 2.2%, compared to the previous result 12%. Pressure profiles with sharper boundaries have lower beta limits. The equilibrium is governed by the predominant quadrupole Pfirsch-Schlüter current. Small deviations from the CREL condition have almost no effects on the equilibrium, and thus the beta limit. Possible ways of raising the beta limit are also discussed.

1. INTRODUCTION

A DRAKON [1,2] (a Russian acronym for long equilibrium configuration) is a closed-end magnetic confinement system that contains two long straight sections (s.s.) of low magnetic field, joined at the ends by two special connectors of high magnetic field. These special connectors are called "CRELs" (Connector of Rectilinear ELements). They satisfy the so called CREL condition and in general have three-dimensional curvilinear configurations. A conceptual coil set design of a DRAKON with triangular CRELs is shown in Fig. 1.

Ideally, the CREL condition guarantees that no parallel plasma currents flow out of the CRELs, thereby keeping the equilibrium in the straight sections autonomous. In a realistic CREL, however, only the lowest-order CREL condition can be satisfied. It prevents the dipole Pfirsch-Schlüter current from flowing out of the CRELs and therefore the first-order (in plasma beta) shift is independent of the lengths of the straight sections. Different designs of this type of CRELs have been presented in Ref. [1,3]. Among them, the simplest one is the triangular CREL, which is made up of three semitori twisted at the joints by 120°. Based only on the first-order shift, the peak equilibrium beta limit β^* was estimated to be about 12% in the triangular CRELs [1]. (Note that the beta limit given there was the average one, which was half the peak beta for a parabolic pressure profile.) Since the beta in the straight sections is scaled up by the square of the mirror ratio, this estimate can lead to a favorably high beta in the straight sections. This may be overoptimistic: the higher-order distortions, which do depend on the straight section length, may dominate over the first-order shift, resulting in lower beta limits. Observing this, Makurin and Mikhailovskii carried out the calculation to third order in beta [4]. Nevertheless, the beta limit for a specific CREL was not evaluated. Only some rough estimates were given. The conclusion was that if the straight sections did not exceed the CRELs in length, the first-order beta limit remained true.

Here we follow the same line as Makurin and Mikhailovskii did, but generalize their calculation to systems that do not necessary satisfy the CREL condition. This allows us to investigate the effects of deviations from the CREL condition (imperfect CRELs). Besides, the formulas to second-order are valid for arbitrary pressure profiles. Thus the effects of different pressure profiles can be studied easily. (A parabolic pressure profile were used in Ref. [4].) For the special case of a DRAKON with triangular CRELs, an analytic formula of the second-order (including the dominant terms in the elliptical distortion) beta limit is derived. The predictions of this formula are compared with the numerical evaluations of the full expressions to third order. Through this a semi-analytic formula for the beta limit in DRAKONs with triangular CRELs is obtained.

The coordinate systems, various expansions, and some basic equations are given in Sec. 2. The

boundary conditions at the throats—the joints between straight sections and CRELs—are discussed in Sec. 3. The shift and elliptical distortion are then solved in Sec. 4, the results being applicable to DRAKONs with arbitrary connectors and arbitrary pressure profiles. For the special case of a DRAKON with triangular CRELs, an analytic formula of the second-order beta limit is derived in Sec. 5. The full expressions to third order for DRAKONs with imperfect CRELs are given in Sec. 6. In Sec. 7, numerical evaluations of these expressions for a triangular-CREL DRAKON with parabolic pressure profile yield the flux surface plots. The effects of deviations from the CREL condition are investigated. The numerical beta limits are compared with the analytic ones, leading to a semi-analytic formula. Finally, conclusions and discussion are given in Sec. 8.

2. COORDINATES AND BASIC EQUATIONS

In this section the derivation of the equations for the Pfirsch-Schlüter current and distortion functions is outlined in four steps: (1) set up a coordinate system along the system, (2) introduce the flux coordinates, Fourier expansions, and distortions, (3) find the metric coefficients g_{ij}, (4) obtain equations for the distortions and Pfirsch-Schlüter currents. The mathematical expressions in steps (3) and (4) are quite lengthy. We will only give the outline and some lowest-order expressions here. Details can be found in Ref. [4,5].

The system axis (vacuum magnetic axis) of an arbitrary system is a spatial curve described by the Frenet-Serret equations

$$\frac{d\vec{t}}{ds} = k\vec{n}, \tag{1a}$$

$$\frac{d\vec{n}}{ds} = -k\vec{t} + \kappa\vec{\beta}, \tag{1b}$$

$$\frac{d\vec{\beta}}{ds} = -\kappa\vec{n}, \tag{1c}$$

where s is the arc length of the system axis measured from some reference point. The normal, binormal, and tangential unit vectors $(\vec{n}, \vec{\beta}, \vec{t})$ form an orthonormal base along this axis (Fig. 2). The curvature of the axis $k(s) \geq 0$ by definition. The torsion of the axis is $\kappa(s)$. We will use an angle-like variable $\zeta = s/R$ to specify the longitudinal position ($R = L_{\rm tot}/2\pi$ is the effective radius). A polar coordinate system (r, θ) is then set up based on $(\vec{n}, \vec{\beta})$. The length element in these coordinates is

$$dl^2 = dr^2 + r^2 d\theta^2 + 2\kappa r^2 R d\theta d\zeta + (h^2 + \kappa^2 r^2) R^2 d\zeta^2, \tag{2a}$$

with

$$h \equiv 1 - kr\cos\theta. \tag{2b}$$

Next we introduce the flux coordinates $(x^1, x^2, x^3) = (a, \omega, \zeta)$, where a is the radial coordinate and ω the poloidal angle. The magnetic field in these coordinates is

$$\vec{B} = \chi' \nabla\zeta \times \nabla a + \psi' \nabla a \times \nabla\omega. \tag{3a}$$

Here χ and ψ are the poloidal and longitudinal magnetic fluxes divided by 2π. A prime denotes derivative with respect to a. Field lines are straight in the flux coordinates

$$\omega = \frac{\chi'}{\psi'}\zeta + \text{const} = \mu\zeta + \text{const}, \tag{3b}$$

where $\mu = \chi'/\psi'$ is the *rotation number*. The current is

$$\vec{J} = I' \nabla\zeta \times \nabla a + J' \nabla a \times \nabla\omega + \nabla a \times \nabla\nu, \tag{4}$$

where I and J are flux functions related to the poloidal and longitudinal currents, and ν is the Pfirsch-Schlüter current—a current whose average over ω is zero. Ampére's law and the MHD force balance equation in these flux coordinates can be found in Ref. [6].

The magnetic axis, in general, is not the same as the system axis. At a fixed ζ, the origin of the polar coordinates is shifted by $x \exp i\theta_x$. Here the $\vec{n}$ direction is treated as the real axis and $\vec{\beta}$ as imaginary. A new polar coordinates (r_0, θ_0) is now set up with reference to this shifted origin. Thus we have

$$r \exp(i\theta) = x \exp(i\theta_x) + r_0 \exp(i\theta_0). \tag{5}$$

Figure 3 shows the relation between these coordinates. (Note that the notations here are different from those in Ref. [4]: our $r, r_0 \longrightarrow \rho, \rho_0$ there and $\omega \longleftrightarrow \theta$, $\omega_0 \longleftrightarrow \theta_0$.)

The new polar coordinates are now related to the flux coordinates through Fourier expansions,

$$\begin{aligned} \theta_0 &= \omega + H(a,\zeta) + \text{Im}\left(\Lambda e^{i\omega} + M e^{i2\omega} + N e^{i3\omega} + \cdots\right) \\ &\equiv \omega_0 + H(a,\zeta), \end{aligned} \tag{6a}$$

and

$$\begin{aligned} r_0 &= a + \text{Re}\left(\lambda e^{i2\omega_0} + \tau e^{i3\omega_0} + \cdots\right) \\ &= a + \text{Re}\left(\lambda e^{i2\omega} - \lambda\Lambda^* e^{i\omega} + (\lambda\Lambda + \tau) e^{i3\omega} + \cdots\right). \end{aligned} \tag{6b}$$

(The function H is called h in Ref. [4].) The form of Eq. (6a) is justified if we considered the limiting case of a vacuum field, in which the rectification functions $\Lambda(a,\zeta), M(a,\zeta), N(a,\zeta)$ are zero while $H = H_0$ depends only on the torsion of the system axis. In this case, H_0 rectifies the angle $\omega_0 = \omega$ such that field lines are straight in (ω_0, ζ). Equation (6b) states that the circular cross-sections ($r_0 = a$) are deformed by the elliptical distortion $\lambda(a,\zeta)$, the triangular distortion

$\tau(a,\zeta)$, etc. Assuming that the plasma is enclosed by a conducting wall of radius b, ellipticity $\lambda_0(\zeta)$, and triangularity $\tau_0(\zeta)$, we have

$$r_0(b) = b + \mathrm{Re}\Big(\lambda_0(\zeta)e^{i2\omega_0} + \tau_0(\zeta)e^{i3\omega_0} + \cdots\Big). \tag{7}$$

When the plasma pressure is very low, the flux surfaces are shaped solely by the wall.

The shift function $\xi(a,\zeta)$ is defined by

$$\xi^* \exp(iH) \equiv x \exp(i\theta_x). \tag{8}$$

Since the axis of the wall (system axis) has zero shift by definition, we have, together with Eq. (7),

$$\xi(b,\zeta) = 0, \quad \lambda(b,\zeta) = \lambda_0(\zeta), \quad \tau(b,\zeta) = \tau_0(\zeta), \quad \cdots. \tag{9a}$$

Near the magnetic axis, flux surfaces should degenerate to circular tubes surrounding the magnetic axis. Thus,

$$\xi(0,\zeta) \text{ is finite}, \quad \lambda(0,\zeta) = \tau(0,\zeta) = \cdots = 0. \tag{9b}$$

Further, any physical function f should obey the natural periodic boundary condition

$$f(\zeta + 2\pi) = f(\zeta). \tag{9c}$$

Equations (9) are the boundary conditions of the distortion functions.

The third step is to express the metric coefficients in terms of the rectification and distortion functions. This can be done simply be plugging Eqs. (5), (6a), and (6b) into Eq. (2a) and then use

$$dl^2 = \sum_{ij} g_{ij} dx^i dx^j. \tag{10}$$

Results are lengthy and can be found in Ref. [5]. It turns out that g_{33} is a dominant element and Ampére's law in flux coordinates leads to [6]

$$\frac{\partial}{\partial\omega}\frac{g_{33}}{\sqrt{g}} = 0. \tag{11}$$

Different Fourier components of this equation can then be used to express Λ, M, and N in terms of H, ξ, λ, and τ.

Finally, to obtain the equations for the distortions, we Fourier decompose the Pfirsch-Schlüter current

$$\nu = \mathrm{Re}\Big(\nu^{(1)}e^{i\omega} + \nu^{(2)}e^{i2\omega} + \nu^{(3)}e^{i3\omega} + \cdots\Big). \tag{12}$$

Then different harmonics of Ampére's law yield (all the formulas are in cgs units)

$$\left(\mu - i\frac{\partial}{\partial\zeta}\right)\left(\xi_1'' + \frac{3}{a}\xi_1'\right) = -\frac{i2R}{a\psi'}\frac{4\pi}{c}\nu_1^{(1)}, \tag{13a}$$

$$\left(2\mu - i\frac{\partial}{\partial\zeta}\right)\left(\lambda'' + \frac{3}{a}\lambda' - \frac{3}{a^2}\lambda\right) = -\frac{i8R}{a\psi'}\frac{4\pi}{c}\nu_2^{(2)}, \tag{13b}$$

where the subscripts of ν and ξ denote the order in β. Note that those terms proportional to ξ_1^2 on the right hand side of Eq. (13b) are left out. They are small compared to $\nu_2^{(2)}$, as will be shown later by comparison of the analytic and numerical results. Furthermore, it is sufficient to use the zeroth-order rotation number μ_0 , which is

$$\mu_0 = \frac{4\pi}{c}\frac{JR}{\psi' a} - \kappa_0 R \tag{14}$$

with

$$\kappa_0 \equiv \oint \frac{d\zeta}{2\pi}\kappa. \tag{15}$$

Similarly, the equations for $\nu^{(n)}$ are found from different harmonics of the force balance equation. The first two are

$$\left(\mu - i\frac{\partial}{\partial\zeta}\right)\nu_1^{(1)} = -i\frac{a^2}{\psi'}cP'Rke^{iH}, \tag{16a}$$

$$\left(2\mu - i\frac{\partial}{\partial\zeta}\right)\nu_2^{(2)} = i\frac{a^2}{2\psi'}cP'Rk\xi_1'. \tag{16b}$$

As before, we can use μ_0 and H_0 in these equations. The zeroth-order H is

$$H_0 = R\int_0^\zeta(\kappa_0 - \kappa)d\zeta. \tag{17}$$

All the harmonics of the Pfirsch-Schlüter current $\nu^{(n)}$ should obey the natural periodic boundary condition Eq. (9c).

3. BOUNDARY CONDITIONS AT THE THROATS

In Makurin and Mikhailovskii's paper [4], the boundary conditions at the throats were not given. Here from current continuity, we derive those boundary conditions necessary for obtaining ν and the distortion functions.

For a given flux surface, its radius in the straight sections is not the same as in the CRELs if the mirror ratio $R_M > 1$. They are related by

$$\frac{a_{\rm ss}}{a_{\rm CR}} = \sqrt{R_M}. \tag{18}$$

For simplicity, we will ignore any transition regions between the straight sections and the CRELs. Thus B increases suddenly by a factor of R_M when entering the CRELs from the straight sections. The differential equations for $\nu^{(n)}$ and the distortions derived in Sec. 2 will be solved piecewise and then jointed together through boundary conditions at the throats.

First is the Pfirsch-Schlüter current. In the flux coordinates (a, ω, ζ), ν has the dimension of a surface current. We set up a closed surface with two adjacent flux surfaces and two constant-ζ annuli, one in the straight section, the other in the CREL (Fig. 4). Then we apply the integral form of the current continuity equation on this surface. Since $\vec{J}$ does not flow out of the flux surfaces, the only requirement from continuity is that $J_\zeta 2\pi a da$ be the same on the two annuli. Noting that the longitudinal current $J' = 0$ in a DRAKON, we have from Eq. (4)

$$\frac{1}{a}\frac{\partial \nu}{\partial \omega} 2\pi a da = \text{const} \tag{19a}$$

across the throat. After Fourier expansion, it becomes

$$\nu^{(n)} da = \text{const.} \tag{19b}$$

Thus $\nu^{(n)}$ is decreased by a factor of $\sqrt{R_M}$ as it enters the straight section.

Next we turn to the shift equation (13a). The jump in $\nu_1^{(1)}$ also generates a jump in ξ_1. Observing that $a\psi'$ and $a\nu_1^{(1)}$ remain the same on both sides of the throat, we find that ξ_1' is also the same on both sides. Hence ξ_1 is enlarged by a factor of $\sqrt{R_M}$ as we go into the straight section from the CREL. For the special case of $R_M = 1$, ξ_1 should be continuous at the throat. This fact is used to determine the integral constant from solving Eq. (13a) with respect to ζ. The same argument apply to other distortions as well. Thus we arrive at the conclusion: ***all distortions are scaled up by a factor of $\sqrt{R_M}$ when entering the straight section from the CREL.*** In practice, we will solve the equations for the special case $R_M = 1$ and then use these boundary conditions to obtain the solutions in the straight section.

4. SOLUTIONS OF THE SHIFT AND ELLIPTICAL DISTORTION

Unless otherwise specified, the plasma beta (and beta limit) is the peak beta in the CRELs

$$\beta = \frac{8\pi P(0)}{B_{\text{CR}}^2} = \frac{8\pi P(0) a_{\text{CR}}^2}{\psi'^2}. \tag{20}$$

As explained in Sec. 3, we first deal with $R_M = 1$, in which case all $\nu^{(n)}$ and distortions are continuous functions of ζ. Besides the 2π-periodicity [Eq. (9c)], all physical functions ($\nu^{(n)}, H, \xi, \lambda, \tau$, etc.) actually possess π-periodicity

$$f(\zeta + \pi) = f(\zeta). \tag{21}$$

This is because we choose the two CRELs on both sides to be identical. It also implies that the curvature and torsion of the DRAKON satisfy

$$k(\zeta + \pi) = k(\zeta), \quad \text{and} \quad \kappa(\zeta + \pi) = \kappa(\zeta). \tag{22}$$

Other geometric functions appearing in Eq. (7), such as b, λ_0, etc., all have the same π-periodicity. This π-periodicity is quite useful for checking the correctness of the solutions and evaluating the integration constants.

Noticing that $J = 0$ in a DRAKON (current-free system), we can use Eq. (14) to rewrite Eq. (17) as

$$H_0 = -\mu_0\zeta - \alpha_0(\zeta), \tag{23}$$

where

$$\alpha_0 = R\int_0^\zeta \kappa d\zeta = \int_0^s \kappa ds \tag{24a}$$

is the twisting angle of the system axis. The zeroth-order rotational transform is given by

$$\iota_0 = -\alpha_0(2\pi) = 2\pi\mu_0. \tag{24b}$$

With Eq. (23), it is straightforward to solve Eq. (16a) to obtain

$$\nu_1^{(1)} = \frac{\beta\psi'}{2}\frac{c}{4\pi}\hat{P}'(a)\Big(A^{(1)} + D(\zeta)\Big)\exp(-i\mu_0\zeta), \tag{25}$$

where

$$\hat{P}(a) = \frac{P(a)}{P(0)}, \tag{26}$$

and

$$D(\zeta) = R\int_0^\zeta d\zeta k\exp(-i\alpha_0). \tag{27}$$

The integration constant is found from the natural periodic boundary condition Eq. (9c) to be

$$A^{(1)} = -\frac{i\exp(-i\pi\mu_0)}{2\sin(\pi\mu_0)}D(2\pi). \tag{28}$$

Plugging Eq. (25) into Eq. (13a) and observing that Eq. (13a) is an Euler-typed equation with respect to a, we solve it by the method of Green's function to obtain

$$\frac{\xi_1}{b} = -\left(\frac{\beta l}{4b}\right)R_{\xi_1}(a)\mathrm{CADF}(\zeta)\exp(-i\mu_0\zeta). \tag{29}$$

Here l is the length of one CREL. The radial function

$$R_{\xi_1}(a) \equiv -2\left(\hat{P}(a) - \hat{P}(b) - \frac{1}{a^2}\int_0^a daa^2\hat{P}'(a) + \frac{1}{b^2}\int_0^b daa^2\hat{P}'(a)\right). \tag{30}$$

And the axial function

$$\mathrm{CADF}(\zeta) \equiv \hat{C}_1 + \frac{R\zeta}{l}(A^{(1)} + D(\zeta)) - \hat{F}(\zeta), \tag{31}$$

with

$$\hat{F}(\zeta) \equiv \frac{R^2}{l}\int_0^\zeta d\zeta\zeta k\exp(-i\alpha_0). \tag{32}$$

The integration constant is

$$\hat{C}_1 = \frac{i\exp(-i\pi\mu_0)}{2\sin(\pi\mu_0)}\hat{F}(2\pi) - \frac{R}{l}\frac{2\pi D(2\pi)}{4\sin^2(\pi\mu_0)}. \tag{33}$$

Eqs. (25) and (29) can be shown to have the correct π-periodicity.

To obtain the shift for $R_M > 1$, we simply replace $(\beta l/4b)$ by $(\beta l/4b_{\rm CR})$ in Eq. (29) with other b's unchanged. Since

$$b = \begin{cases} b_{\rm CR} & \text{in CREL.} \\ b_{\rm ss} = \sqrt{R_M} b_{\rm CR} & \text{in s.s.} \end{cases} \tag{34}$$

The resulting ξ_1 then has the correct scaling when entering the straight sections from the CRELs.

Now we proceed to the second-order equations. The derivative

$$\frac{\xi_1'}{b} = \frac{\beta l}{b}\left(\frac{1}{a^3}\int_0^a daa^2\hat{P}'\right)\mathrm{CADF}(\zeta)\exp(-i\mu_0\zeta) \tag{35}$$

is put into Eq. (16b) to produce

$$\nu_2^{(2)} = -\frac{\beta^2\psi' l}{4}\frac{c}{4\pi}\left(\frac{\hat{P}'}{a^3}\int_0^a daa^2\hat{P}'\right)\left(\hat{C}^{(2)} + \hat{N}^{(2)}(\zeta)\right)\exp(-i2\mu_0\zeta). \tag{36}$$

Here

$$\hat{N}^{(2)}(\zeta) \equiv D(\zeta)\mathrm{CADF}(\zeta) - \frac{R}{l}\int_0^\zeta d\zeta(A^{(1)} + D)D, \tag{37}$$

and

$$\hat{C}^{(2)} = -\frac{i\exp(-i2\pi\mu_0)}{2\sin(2\pi\mu_0)}\hat{N}^{(2)}(2\pi). \tag{38}$$

Equation (13b) is then solved as before, resulting in

$$\frac{\lambda}{b} = \left(\frac{\beta l}{2b_{\rm CR}}\right)^2 R_{\lambda\nu}(a)8\mathrm{CCN}(\zeta)\exp(-i2\mu_0\zeta). \tag{39}$$

Here the radial function

$$R_{\lambda\nu}(a) \equiv -\frac{b}{4}\left(a\int_b^a da\frac{\hat{P}'}{a^4}\int_0^a daa^2\hat{P}' - \frac{1}{a^3}\int_0^a da\hat{P}'\int_0^a daa^2\hat{P}' + \frac{a}{b^4}\int_0^b da\hat{P}'\int_0^a daa^2\hat{P}'\right), \tag{40}$$

and the axial function

$$\mathrm{CCN}(\zeta) \equiv \hat{C}_\lambda + \frac{R}{l}\int_0^\zeta d\zeta\left(\hat{C}^{(2)} + \hat{N}^{(2)}(\zeta)\right). \tag{41}$$

The integration constant is

$$\hat{C}_\lambda = -\frac{i\exp(-i2\pi\mu_0)}{2\sin(2\pi\mu_0)}\frac{R}{l}\left(2\pi\hat{C}^{(2)} + \int_0^{2\pi} d\zeta\hat{N}^{(2)}\right). \tag{42}$$

In addition, we have chosen a circular wall, so that $\lambda_0 = 0$.

So far, our solutions are valid for arbitrary connectors. A CREL satisfies the CREL condition

$$\nu_1^{(1)} = 0 \quad \text{at the throats.} \tag{43}$$

Since $D(\zeta) = D(2\pi) = D(\pi)$ in the straight sections, the CREL condition requires that

$$A^{(1)} = 0 \quad \text{or} \quad D(2\pi) = D(\pi) = 0. \tag{44}$$

Thus

$$\hat{C}_1 = \frac{i\exp(-i\pi\mu_0)}{2\sin(\pi\mu_0)}\hat{F}(2\pi). \tag{45}$$

Once the CREL condition is satisfied, the shift ξ_1 is independent of the length L of the straight sections. The same statement, however, does not hold for the elliptical distortion λ. A beta limit to second order (including the elliptical distortion) will therefore depend on L, as we shall see in Sec. 5.

5. AN ANALYTIC FORMULA FOR THE SECOND-ORDER EQUILIBRIUM BETA LIMIT

In the original paper [1] that proposed the DRAKON, a formula based only on the first-order shift ξ_1 was used to estimate the peak beta limit β^*, leading to the favorable result of $\beta^* \sim 12\%$ in the CREL. (Note that the beta limit given there was the average one, which was half the peak beta for a parabolic pressure profile.) This was overoptimistic. It is the elliptical distortion λ, which is driven by the quadrupole Pfirsch-Schlüter current, that plays a more important role than ξ_1. A beta limit that includes λ will therefore be much lower than that without. In this section, we will derive an analytic formula for the second-order equilibrium beta limit in DRAKONs with triangular CRELs. The formula is good for arbitrary radial pressure profile. Thus the effects of different pressure profiles can be investigated easily. In Sec. 7, the prediction of this formula will also be used to cross-check the numerical results.

The DRAKON we consider here is perfect, in the sense that its curvature k is made up of step functions

$$k(s) = \begin{cases} k_0 & 0 < s < l \\ 0 & l < s < l + L \\ k_0 & l + L < s < 2l + L \\ 0 & 2l + L < s < 2(l + L) \end{cases} \tag{46}$$

($k_0 = 1/R_0 = 3\pi/l$, l being the length of one CREL, L that of one straight section), and its torsion κ of δ functions

$$\kappa(s) = \alpha_{ss}\delta(s) - \alpha_{CR}[\delta(s - l/3) + \delta(s - 2l/3)] + \alpha_{ss}[\delta(s - l) + \delta(s - l - L)]$$

$$- \alpha_{CR}[\delta(s - 4l/3 - L) + \delta(s - 5l/3 - L)] + \alpha_{ss}\delta(s - 2l - L), \tag{47a}$$

with

$$\alpha_{CR} = 120^\circ, \quad \alpha_{ss} = 19.11^\circ. \tag{47b}$$

The rotational transform of the system axis is

$$\iota_0 = -\oint \kappa ds = 4(\alpha_{CR} - \alpha_{ss}) = 403.56^\circ. \tag{48}$$

We first calculate the three integration constants $\hat{C}_1, \hat{C}^{(2)}$, and $\hat{C}_\lambda$. From Eqs. (45) and (22) it is not hard to show

$$\hat{C}_1 = \frac{i\exp(-i\pi\mu_0/2)}{2\sin(\pi\mu_0/2)}\hat{F}(\pi). \tag{49}$$

To simplify notations, we will make $R\zeta/l \to s$ and $kl \to k$. After one integration by parts on $\hat{F}$, Eq. (49) becomes

$$\hat{C}_1 = \frac{-i}{2\sin(\pi\mu_0/2)}\int_0^1 ds D(s)\exp(-i\pi\mu_0/2). \tag{50}$$

Noting that $-\pi\mu_0/2 = \alpha_{ss} - \alpha_{CR}$, we plot $D(s)\exp(-i\pi\mu_0/2)$ and $\alpha_0 + \pi\mu_0/2$ in Fig. 5. Different segments of $D(s)\exp(-i\pi\mu_0/2)$ are represented by

$$D(s)\exp(-i\pi\mu_0/2) = \begin{cases} 3\pi s\exp(-i2\pi/3) & 0 \le s < 1/3 \\ 3\pi(s - 1/2) - i\pi\sqrt{3}/2 & 1/3 \le s < 2/3 \\ 3\pi(1 - s)\exp(-i\pi/3) & 2/3 \le s < 1. \end{cases} \tag{51}$$

Since it is a linear function of s, its integral over s is just the center of mass of an equilateral triangular wire with side length $1/3$ and uniformly distributed mass π on each side. Hence, by finding the center of mass of the wire, we obtain

$$\hat{C}_1 = \frac{-\pi}{2\sqrt{3}\sin(\pi\mu_0/2)} = -0.9235. \tag{52}$$

This is a real number, as can easily be justified from Fig. 5(a).

Next is the constant $\hat{C}^{(2)}$. Again, the use of the π-periodicity yields

$$\begin{aligned} \hat{C}^{(2)} &= -\frac{i\exp(-i\pi\mu_0)}{2\sin(\pi\mu_0)}\hat{N}^{(2)}(\pi) \\ &= \frac{i}{2\sin(\pi\mu_0)}\int_0^1 ds[D(s)\exp(-i\pi\mu_0/2)]^2 . \end{aligned} \tag{53}$$

The function $[D(s)\exp(-i\pi\mu_0/2)]^2$ is plotted in Fig. 6. Since $|D(s)| = |D(1 - s)|$, the average of this function must be real. Thus,

$$\hat{C}^{(2)} = \frac{i}{\sin(\pi\mu_0)}\mathrm{Re}\int_0^{1/2} ds[D(s)\exp(-i\pi\mu_0/2)]^2 .$$

Now it is straightforward to use Eq. (51) to obtain

$$\hat{C}^{(2)} = \frac{-i\pi^2}{6\sin(\pi\mu_0)} = 4.433i. \tag{54}$$

Finally, the constant $\hat{C}_\lambda$ after applying the π-periodicity and partial integrations is

$$\begin{aligned}\hat{C}_\lambda &= -\frac{i\exp(-i\pi\mu_0)}{2\sin(\pi\mu_0)}\left(\pi\hat{C}^{(2)}\frac{\hat{L}+1}{\pi} + \int_0^1 ds\hat{N}^{(2)}\right) \\ &= (\hat{L}+1)\frac{-i\exp(i\pi\mu_0)}{2\sin(\pi\mu_0)}\hat{C}^{(2)} + \hat{C}_{\lambda 0},\end{aligned} \tag{55}$$

where $\hat{L} = L/l$ and

$$\begin{aligned}\hat{C}_{\lambda 0} &= -\frac{i\exp(-i\pi\mu_0)}{2\sin(\pi\mu_0)}\int_0^1 dsD(\mathrm{CADF} + sD) \\ &= -\frac{i\exp(-i\pi\mu_0)}{2\sin(\pi\mu_0)}\int_0^1 dsD\left(\hat{C}_1 + \int_0^s ds'D(s') + sD\right).\end{aligned} \tag{56}$$

The three terms in the second expression of Eq. (56) are evaluated as follows. With Eq. (50),

$$\text{the first term} = \frac{\exp(-i\pi\mu_0/2)}{2\cos(\pi\mu_0/2)}\hat{C}_1^2. \tag{57}$$

Likewise,

$$\begin{aligned}\text{the second term} &= \frac{i}{2}\tan(\frac{\pi\mu_0}{2})\left(\frac{-i\exp(-i\pi\mu_0/2)}{2\sin(\pi\mu_0/2)}\int_0^1 dsD\right)^2 \\ &= \frac{i}{2}\tan(\frac{\pi\mu_0}{2})\hat{C}_1^2.\end{aligned} \tag{58}$$

The last term is integrated first by parts and then with Eq. (51).

$$\begin{aligned}\text{The last term} &= \frac{ik_0}{2\sin(\pi\mu_0)}\int_0^1 dss^2D\exp(-i\pi\mu_0/2)\exp[-i(\alpha_0+\pi\mu_0/2)] \\ &= \frac{i\pi^2}{2\sin(\pi\mu_0)}\left(\frac{1}{6} + \frac{i}{9\sqrt{3}}\right).\end{aligned} \tag{59}$$

Summing them up and substituting $\hat{C}_1$ with Eq. (52), we obtain

$$\begin{aligned}\hat{C}_{\lambda 0} &= \frac{\pi^2}{24\sin^2(\pi\mu_0/2)} + \frac{\pi^2}{2\sin(\pi\mu_0)}\left(-\frac{1}{9\sqrt{3}} + \frac{i}{6}\right) \\ &= 1.280 - 2.217i.\end{aligned} \tag{60}$$

Thus

$$\hat{C}_\lambda = (\hat{L}+1)(5.548 + 2.217i) + (1.280 - 2.217i). \tag{61}$$

This constant has an imaginary part proportional to $\hat{L}$. Since $\hat{C}_1$ is real, this means that at the the origin the relative phase between the shift and the elliptical distortion depends on $\hat{L}$ too.

The beta limit β^* is defined to be the beta value at which the inner flux surfaces start to cross the outer ones. Flux surfaces cross each other first at those points where various distortions are constructive. To second order, this means that at the origin ξ_1 and λ are in phase or have a phase difference of π. The β^* to second order can therefore be obtained by considering the shift and elliptical distortion at such points. It is found that the center of the straight section is a point of this type. To show this, we shift the origin $\zeta = 0$ from the throat to the center of the straight section. Both $\hat{C}_1$ and $\hat{C}^{(2)}$ are not affected by this shift because $D = 0$ in the straight section. For the same reason, the new $\hat{C}_\lambda$ is

$$\begin{aligned}\hat{C}'_\lambda &= (\hat{L}+1)\frac{-i\exp(i\pi\mu_0)}{2\sin(\pi\mu_0)}\hat{C}^{(2)} - \frac{\hat{L}}{2}\hat{C}^{(2)} + \hat{C}_{\lambda 0} \\ &= (\hat{L}+1)\frac{-\pi^2\cot(\pi\mu_0)}{12\sin(\pi\mu_0)} + \pi^2\left(\frac{1}{24\sin^2(\pi\mu_0/2)} - \frac{1}{18\sqrt{3}\sin(\pi\mu_0)}\right) \\ &= (\hat{L}+1)5.548 + 1.280, \end{aligned} \tag{62}$$

which is a real number!

At the new origin $\zeta' = 0$, ξ_1 is in the $-\vec{n}$ direction. λ bulges out in the same direction too. Thus in this direction,

$$r(a,0) = a - \xi_1(a,0) + \lambda(a,0). \tag{63}$$

A schematic of $r(a)$ is plotted in Fig. 7. At $\beta = 0$, it is simply $r = a$. When β is raised, distortions make r bigger, while $r(b) = b$ is fixed. Since the gradient of the radial pressure profile is in general higher in the outer region than in the inner one, the r in the outer region will be driven to a bigger value faster than that in the inner one. When $\beta > \beta^*$, part of the outer region has $r > b$, which means that the flux surfaces there have already crossed the wall. Thus the first sign for this to happen is when

$$r'(b) = 1 - \xi_1'(b) + \lambda'(b) = 0, \tag{64}$$

where the prime denotes d/da. Equation (64) as a quadratic algebraic equation for β yields the beta limit β^*.

Using Eq. (35) and the a derivative of Eq. (39) with $a = b$, $\zeta \to \zeta' = 0$, and $\hat{C}_\lambda \to \hat{C}'_\lambda$ in Eq. (64) gives

$$1 - \left(\frac{\beta^* l}{b_{\rm CR}}\right)\frac{\hat{C}_1}{b^2}\int_0^b daa^2\hat{P}' + \left(\frac{\beta^* l}{b_{\rm CR}}\right)^2 2\hat{C}'_\lambda b R'_{\lambda\nu}(b) = 0, \tag{65}$$

where from Eq. (40),

$$\begin{aligned} bR'_{\lambda\nu}(b) &= -\frac{1}{b^2}\int_0^b da\hat{P}'\int_0^b daa^2\hat{P}' \\ &= -\frac{1}{b^2}\int_0^b daa\hat{P}^2 - \frac{\hat{P}^2(b)}{2} + \frac{\hat{P}(b)}{2b^2}\int_0^b daa\hat{P}. \end{aligned} \tag{65b}$$

For the special case of a parabolic pressure profile

$$\hat{P}(a) = 1 - \frac{a^2}{b^2}, \tag{66}$$

Eq. (65) becomes

$$1 + \left(\frac{\beta^* l}{b_{\rm CR}}\right)\frac{\hat{C}_1}{2} - \left(\frac{\beta^* l}{b_{\rm CR}}\right)^2 \frac{\hat{C}'_\lambda}{3} = 0. \tag{67}$$

The old beta limit [1] is obtained by ignoring the β^2 term in this equation, yielding

$$\beta^* = -\frac{2b_{\rm CR}}{\hat{C}_1 l} = 11.5\% \quad (\text{for } k_0 b = 0.5), \tag{68}$$

which is independent of $\hat{L}$. Now the β^* to second order obtained from Eq. (67) is

$$\beta^* = \frac{b_{\rm CR}}{l}\frac{\left[29.59(\hat{L}+1) + 7.678\right]^{1/2} - 0.9235}{7.398(\hat{L}+1) + 1.706}, \tag{69}$$

This β^* is considerably lower than the first-order one [Eq. (68)]. For example, $\beta^* = 2.33\%$ for $\hat{L} = 1$ and $k_0 b = 0.5$. This is because the quadrupole Pfirsch-Schlüter current is much larger than the dipole one ($|\hat{C}'_\lambda| \gg |\hat{C}_1|$). The equilibrium and therefore the beta limit is determined mainly by the elliptical distortion.

The effects of the pressure profile can also be investigate easily from Eq. (65). Two pressure profiles are used: $\hat{P} = (1 - \hat{a}^g)$ and $\hat{P} = \tanh((1-\hat{a})/g)/\tanh(1/g)$, where $\hat{a} = a/b$. Scanning the free parameter g, we plot β^* versus $-d\hat{P}/d\hat{a}$ at $\hat{a} = 1$ in Fig. 8. The beta limit for the second profile is slightly lower because its gradient is slightly bigger in the interior. Also, beta limits for sharp boundary profiles (large gradients at the wall) are about half of those for smooth profiles.

Finally, although the center of a straight section is found to be a point where the effects of ξ_1 and λ are constructive, it is possible that other points in the CRELs are of this type too. If such points exist, it remains to be answered whether they give a more stringent beta limit or not. Besides, are the second-order driving terms that are proportional to ξ_1^2 and the third-order distortions important? Instead of pursuing the formidable analytic calculations, we will tackle these problems in a combined analytic and numerical way in the following Sections.

6. COMPLETE SOLUTIONS TO THIRD ORDER

In Sec. 4 we discussed in detail how to solve the shift and elliptical distortion. Other distortions can be solved in exactly the same way. Relevant differential equations were given in Ref. [4]. Since they are quite long we will only list the results here. The results here are valid for arbitrary connectors—not necessary CRELs. This makes it possible to investigate the effects of deviations from the CREL condition.

The solutions up to second order are valid for arbitrary pressure profiles. The shift is

$$\frac{\xi_1}{b} = -\left(\frac{\beta l}{4b_{\rm CR}}\right) R_{\xi_1}(a)\mathrm{CADF}(\zeta)\exp(-i\mu_0\zeta), \tag{70a}$$

where the functions R_{ξ_1} and CADF are defined in Eqs. (30) and (31). For the special case of a parabolic profile [Eq. (66)],

$$\frac{\xi_1}{b} = -\left(\frac{\beta l}{4b_{\rm CR}}\right)\left(\frac{a^2}{b^2} - 1\right)\mathrm{CADF}(\zeta)\exp(-i\mu_0\zeta). \tag{70b}$$

We mentioned in Sec. 2 that driving terms proportional to ξ_1^2 were left out of Eq. (13b). Had we included these terms and the λ_0 term, Eq. (39) would become

$$\frac{\lambda}{b} = \left(\frac{\beta l}{2b_{\rm CR}}\right)^2\left[8R_{\lambda\nu}(a)\left(\mathrm{CCN}(\zeta) - \mathrm{CADF}^2\right) + 3R_{\lambda\xi}\mathrm{CADF}^2\right]\exp(-i2\mu_0\zeta) + \frac{a\lambda_0}{b^2}, \tag{71}$$

with

$$R_{\lambda\xi} \equiv -\frac{b}{3a^5}\left(\int_0^a daa^2\hat{P}'\right)^2 + \frac{a}{3b^5}\left(\int_0^b daa^2\hat{P}'\right)^2 - \frac{2ab}{3}\int_b^a da\frac{\hat{P}'}{a^4}\int_0^a a^2\hat{P}'da + 4R_{\lambda\nu}. \tag{72}$$

For the parabolic profile,

$$\frac{\lambda}{b} = \left(\frac{\beta l}{2b_{\rm CR}}\right)^2\frac{a}{12b}\left(1 - \frac{a^2}{b^2}\right)\left(8\mathrm{CCN}(\zeta) - 5\mathrm{CADF}^2\right)\exp(-i2\mu_0\zeta) + \frac{a\lambda_0}{b^2}. \tag{73}$$

The second order of the function H is

$$H_2 = -\frac{1}{2}\left(\frac{\beta l}{2b_{\rm CR}}\right)^2 R_h(a)\frac{R}{l}\left(\hat{M}^{(0)}\zeta - \int_0^\zeta \hat{M}d\zeta\right). \tag{74a}$$

Here the radial function

$$\begin{aligned} R_h(a) &\equiv \left(\frac{2b}{a^3}\int_0^a daa^2\hat{P}'\right)^2 \\ &= a^2/b^2 \quad \text{for the parabolic profile,} \end{aligned} \tag{74b}$$

and the function

$$\hat{M}(\zeta) \equiv \mathrm{Im}\left[(A^{(1)} + D)^*(\hat{C}_1 - \hat{F})\right], \tag{74c}$$

with its average

$$\hat{M}^{(0)} = \frac{1}{2\pi}\int_0^{2\pi}\hat{M}d\zeta. \tag{74d}$$

When calculations are carried out to third order, the expressions become considerably more lengthy. Thus we will only deal with the parabolic pressure profile. The corresponding beta limits to third order are found numerically in Sec. 7, and then compared with the second-order analytic results of Sec. 5. If they agree well, then the results for different pressure profiles obtained in Sec. 5 are good approximations even to third order.

The third-order shift is

$$\frac{\xi_3}{b} = \left(\frac{\beta l}{2b_{\rm CR}}\right)^3 \exp(-i\mu_0\zeta)\left\{\frac{(a/b)^2-1}{8}\left[\frac{\rm CADF^*}{3}(5{\rm CADF}^2 - 8{\rm CCN}) + \frac{R}{l}(\hat{P}_1 + \hat{C}_{P1})\right]\right.$$
$$+ \frac{(a/b)^4-1}{24}\left[\left(4{\rm CCN} - \frac{3}{2}{\rm CADF}^2\right){\rm CADF}^* + \frac{R}{l}(\hat{P}_2 + \hat{C}_{P2})\right.$$
$$\left.\left. + \frac{iR}{2l}{\rm CADF}\left(\hat{M}^{(0)}\zeta - \int_0^\zeta \hat{M}d\zeta\right)\right]\right\} - \frac{\lambda_0}{b}\xi_1^*. \tag{75}$$

Here

$$\hat{P}_1(\zeta) \equiv \int_0^\zeta d\zeta\left[-\frac{1}{3}(A^{(1)} + D)^*(5{\rm CADF}^2 - 8{\rm CCN}) - \frac{2R}{l}(\hat{Q}_1 + \hat{C}_{Q1})\right], \tag{76a}$$

$$\hat{P}_2(\zeta) \equiv \int_0^\zeta d\zeta\left[(A^{(1)} + D)^*\left(\frac{5}{2}{\rm CADF}^2 - 8{\rm CCN}\right) + 2i{\rm CADF}(\zeta)\hat{M}^{(0)}\right.$$
$$\left. + \frac{2iR}{l}\left(\hat{M}^{(0)}\zeta - \int_0^\zeta \hat{M}d\zeta\right)(A^{(1)} + D) - \frac{2R}{l}(\hat{Q}_2 + \hat{C}_{Q2})\right], \tag{76b}$$

and

$$\hat{C}_{Pi} = -\frac{i\exp(-i\pi\mu_0)}{2\sin(\pi\mu_0)}\hat{P}_i(2\pi). \tag{77}$$

The Q functions are defined by

$$\hat{Q}_1(\zeta) \equiv \int_0^\zeta d\zeta\left[-\frac{kl}{6}\exp(i\alpha_0)(5{\rm CADF}^2 - 8{\rm CCN})\right], \tag{78a}$$

$$\hat{Q}_2(\zeta) \equiv \int_0^\zeta d\zeta\left[(A^{(1)} + D)^2{\rm CADF}^* + 2kl\exp(i\alpha_0)\left(\frac{1}{2}{\rm CADF}^2 - {\rm CCN}\right)\right], \tag{78b}$$

with

$$\hat{C}_{Qi} = -\frac{i\exp(-i\pi\mu_0)}{2\sin(\pi\mu_0)}\hat{Q}_i(2\pi). \tag{78c}$$

The triangular distortion is

$$\frac{\tau}{b} = \frac{i}{16}\left(\frac{\beta l}{2b_{\rm CR}}\right)^3 \frac{a^2}{b^2}\left(\frac{a^2}{b^2} - 1\right)(\hat{C}_T + T(\zeta))\exp(-i3\mu_0\zeta) + \frac{a^2\tau_0}{b^3}, \tag{79}$$

where

$$T(\zeta) \equiv \frac{7}{2}{\rm CADF}^3 + 20{\rm CADF}(\zeta){\rm CCN}(\zeta)$$
$$- \frac{R}{l}\int_0^\zeta d\zeta\left[\frac{3R}{2l}(-8{\rm CCN} - 4{\rm CADF}^2)kl\exp(-i\alpha_0) - 12{\rm CCN}(\zeta)(A^{(1)} + D)\right]. \tag{80a}$$

The integration constant is

$$\hat{C}_T = \frac{R}{l}\int_0^{2\pi} d\zeta[\cdots]\frac{i\exp(-i3\pi\mu_0)}{2\sin(3\pi\mu_0)}, \tag{80b}$$

with $[\cdots]$ standing for the terms in the square bracket of Eq. (80a).

7. NUMERICAL EVALUATION OF EQUILIBRIUM FLUX SURFACES AND BETA LIMITS

Based on the expressions given in Sec. 6, a computer code is developed to evaluate the distortions and plot the flux surfaces. By varying the beta interactively and judging from the plots, we can also find the beta limit. Although the code can work with arbitrary input geometric functions (k and α_0), we will only deal with DRAKONs with triangular CRELs here. The origin $\zeta = 0$ is chosen to be the center of a straight section, so that the integration constants from the code can be compared with those from analytic calculation. This also avoids the problem of having functions with sharp transitions, like k and α_0, at the start and the end of the grid mesh. The number of grids around each CREL is six to ten times more than that in each straight section, so as to circumvent the sharp transitions. Integrals are computed with cubic spline quadratures. To test the code, we first check the integration constants. As shown in Table I, the numerical and the analytic results agree to within a relative error of 2%, which is reasonable. Note that this does not necessarily mean the same for the numerical beta limits and the analytic ones [Eq. (69)]. Since the second-order driving terms that are proportional to ξ_1^2 and the third-order distortions had been neglected in Eq. (69).

The first case is a perfect DRAKON with triangular CRELs—one that is made up of step functions (Fig. 9). At four locations along the axis (Fig. 10), the flux surfaces at the beta limit $\beta^* = 2.2\%$ for $k_0 b_{\rm CR} = 0.5$ and $\hat{L} = 1$ are plotted in Fig. 11. All three types of distortions—shift, elliptical and triangular distortions—can be identified clearly. At the origin [Fig. 11(a)], the shift and the elliptical distortion are constructive in the $-\vec{n}$ direction, as was discussed in Sec. 5. Next we consider a more realistic DRAKON in which all the step functions are smoothed out [Fig. 12(a)]. As is shown in Fig. 12(b), the smoothed D function no longer satisfies the CREL condition exactly—the dipole Pfirsch-Schlüter current not vanishing in the straight sections. However, the flux surfaces and the beta limit turn out to be the same. This is not unexpected: according to the finding in Sec. 5 that the quadrupole Pfirsch-Schlüter current dominates over the dipole Pfirsch-Schlüter current, slight changes in the dipole Pfirsch-Schlüter current will have little effects on the equilibrium. When $\hat{L}$ increases, β^* goes down because of larger quadrupole Pfirsch-Schlüter current. The flux surfaces at $\beta^* = 1.3\%$ for $\hat{L} = 5$ are shown in Fig. 13, showing basically the same structure. Figure 14 summarizes the beta limits for different aspect ratios $R_0/b_{\rm CR} = 1/k_0 b_{\rm CR}$ and $\hat{L}$.

To compare these results with the analytic formula Eq. (69), β^* is plotted against $\hat{L}$ in Fig. 14. The dots showing the numerical results are slightly lower than the dashed line resulting from Eq. (69). This confirms that our second-order solutions make the main contribution to β^*. Furthermore, noticing that their difference is almost a constant, we subtract from Eq. (69) a mean

value to obtain the semi-analytic formula

$$\beta^* = \frac{b_{\rm CR}}{l}\frac{\left[29.6(\hat{L}+1)+7.68\right]^{1/2}-0.924}{7.40(\hat{L}+1)+1.71}-.0013. \tag{81}$$

The beta limits from this formula are shown by the solid line in Fig. 15.

8. CONCLUSION AND DISCUSSION

An analytic formula of the second-order equilibrium beta limit for triangular-CREL DRAKONs with arbitrary pressure profile has been derived. For a parabolic pressure profile, its predictions are compared with the full third-order numerical results, leading to a semi-analytic formula that gives the beta limits accurately (Fig. 15). The peak beta limit β^* for different $R_0/b_{\rm CR}$ and $\hat{L} = L/l$ are summarized in Fig. 14. Besides depending on the straight section lengths, these beta limits are considerably lower than the first-order ones; for example, for $R_0/b_{\rm CR} = 2$ and $\hat{L} = 1$, $\beta^* = 2.2\%$. Pressure profiles with sharper boundaries enhance the Pfirsch-Schlüter current and therefore suppress β^* (Fig. 8). The equilibrium is governed by the predominant quadrupole Pfirsch-Schlüter current. Small deviations from the CREL condition (which is better termed *the dipole CREL condition* now, since it eliminates only the dipole Pfirsch-Schlüter current outflow from the CRELs) therefore have almost no effects on the equilibrium, and thus the beta limit.

To raise the equilibrium beta limit, we must suppress the quadrupole Pfirsch-Schlüter current $\nu_2^{(2)}$. A crude way is to alter the twisting angle between the semitori in the CRELs; for instance, when this angle is changed from 120° to 130°, β^* is found numerically to be 3.6% ($R_0/b_{\rm CR} = 2$ and $\hat{L} = 1$). Nonetheless, this change totally destroys the dipole CREL condition. A better way is to eliminate $\nu_2^{(2)}$ in the straight sections while keeping the dipole CREL condition satisfied. This can be achieved by imposing the additional condition—the quadrupole CREL condition

$$\hat{C}^{(2)} = 0, \quad \text{or} \quad \hat{N}^{(2)}(2\pi) = \hat{N}^{(2)}(\pi) = 0 \tag{82}$$

on the CREL. Such a CREL that satisfies both the dipole and quadrupole CREL condition can be called a second-order CREL. Both the shift and elliptical distortion will then be independent of the straight section length. In view of Eq. (37) and the dipole CREL condition, the quadrupole CREL condition can also be written as

$$\int_0^{\pi} d\zeta D^2(\zeta) = 0. \tag{83}$$

The beta limit can be estimated from Eq. (81) by ignoring the $\hat{L}+1$ terms, resulting in $\beta^* = 5.62\%$ ($R_0/b_{\rm CR} = 2$). Whether and how the quadrupole CREL condition can be satisfied by a realistic CREL remain to be answered and will be the subject of future research.

ACKNOWLEDGMENTS

The author would like to thank J. Kesner, K. Brau, J. P. Freidberg, and M. J. Gerver for useful discussions. The coil set design was kindly provided by K. Brau.

This work was supported by the U. S. Department of Energy under Contract No. DE-AC02-78ET51013.

References

[1] V. M. Glagolev, B. B. Kadomtsev, V. D. Shafranov, B. A. Trubnikov, in Controlled Fusion and Plasma Physics (Proc. 10th Europ. Conf. Moscow, 1981), Vol. 1 (1981) paper E-8.

[2] V. V. Arsenin, V. M. Glagolev, B. B. Kadomtsev, V. P. Pastukhov, V. D. Shafranov, B. A. Trubnikov, in Plasma Physics and Controlled Nuclear Fusion Research (Proc. 9th Int. Conf. Baltimore, 1982), Vol. 3, IAEA, Vienna, (1983) 159.

[3] V. M. Glagolev, B. A. Trubnikov, and Yu. N. Churin, Nucl. Fusion **25**, (1985) 881.

[4] S. V. Makurin and A. B. Mikhailovskii, Sov. J. Plasma Phys. **10**, (1984) 171.

[5] Kh. D. Aburdzhaniya and A. B. Mikhailovskii, Sov. J. Plasma Phys. **4**, (1978) 115.

[6] V. D. Shafranov, Nucl. Fusion **8**, (1968) 253.

TABLE I. Integration constants from numerical and analytic calculations.

Constants	$\hat{L}$	Numerical results	Analytic results
$\hat{C}_1$	independent of $\hat{L}$	$-0.928 + 0.002i$	-0.924
$\hat{C}_2$	independent of $\hat{L}$	$0.07 + 4.48i$	$4.43i$
$\hat{C}_\lambda$	1.0	$12.5 - 0.1i$	12.4
	2.5	$20.9 + 0.1i$	20.7
	5.0	$34.5 + 0.1i$	34.6
	10.0	$62.2 - 0.1i$	62.3
	20.0	$117.8 - 1.3i$	117.8

Figures

Fig. 1. A conceptual coil set design of a DRAKON with triangular CRELs. The slot antenna gnerates plasma and the magnetic divertor provides stability.

Fig. 2. Three unit vectors: normal $\vec{n}$, binormal $\vec{\beta}$, and tangential $\vec{t}$.

Fig. 3. Polar coordinates based on the system and the magnetic axes.

Fig. 4. A closed surface made up of two adjacent flux surfaces and two constant-ζ annuli (shaded) is used for applying current continuity. The length of the transition region $\delta\zeta$ is considered to be zero.

Fig. 5. The functions (a) $D(s)\exp(-i\pi\mu_0/2)$ and (b) $\alpha_0 + \pi\mu_0/2$ for a triangular CREL. Note that all lengths are normalized by l.

Fig. 6. The function $[D(s)\exp(-i\pi\mu_0/2)]^2$ for a triangular CREL.

Fig. 7. Schematic of the function $r(a, \zeta' = 0)$. The beta limit β^* is reached when its derivative at b is zero.

Fig. 8. Beta limits as functions of pressure gradient at the wall for different pressure profiles.

Fig. 9. (a) The curvature and twisting angle of a perfect DRAKON with triangular CRELs. (b) The corresponding function D, which is zero in the straight sections.

Fig. 10. Locations and orientations of the flux surface plots in Fig. 11 and 13. Point a to d correspond to plot (a) to (d) in those figures.

Fig. 11. Flux surfaces at the beta limit $\beta^* = 2.2\%$ for a DRAKON with $k_0 b_{\rm CR} = 0.5$ and $\hat{L} = 1$. The surfaces are evenly spaced in the parabolic pressure. See Fig. 10 for their locations and orientations.

Fig. 12. (a) The curvature and twisting angle of a smooth DRAKON with triangular CRELs. (b) The corresponding function D, which is not zero in the straight sections.

Fig. 13. Flux surfaces at the beta limit $\beta^* = 1.3\%$ for a DRAKON with $k_0 b_{\rm CR} = 0.5$ and $\hat{L} = 5$. The surfaces are evenly spaced in the parabolic pressure. See Fig. 10 for their locations and orientations.

Fig. 14. The beta limits for a DRAKON with triangular CRELs.

Fig. 15. Beta limits as a function of $\hat{L}$. The dots are numerical results. The dashed line is from the analytic formula Eq. (69). The solid line corresponds to the semi-analytic formula Eq. (81).

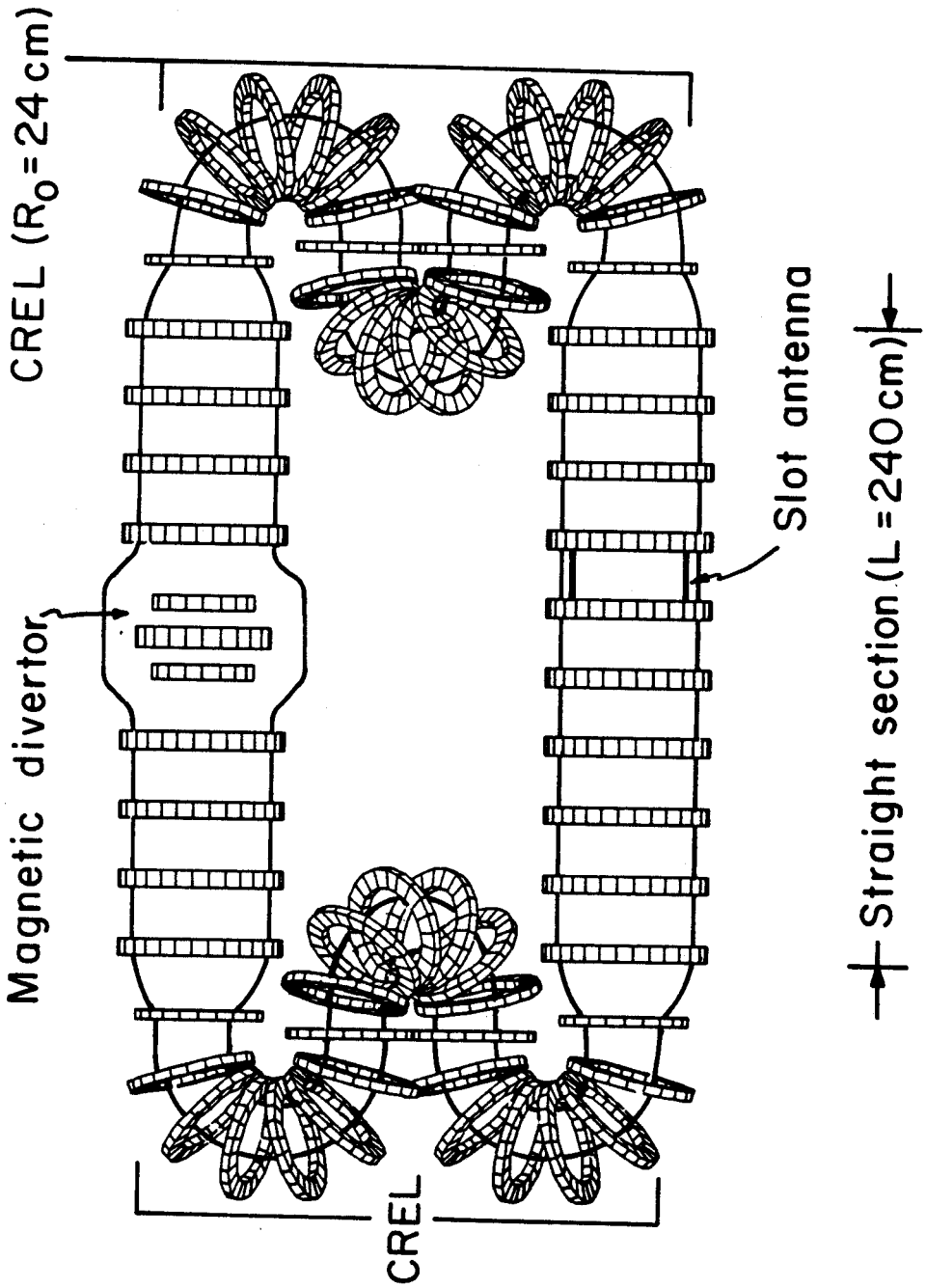
CREL (R_0=24 cm)
Magnetic divertor
Slot antenna
Straight section (L=240 cm)
CREL

Fig. 1

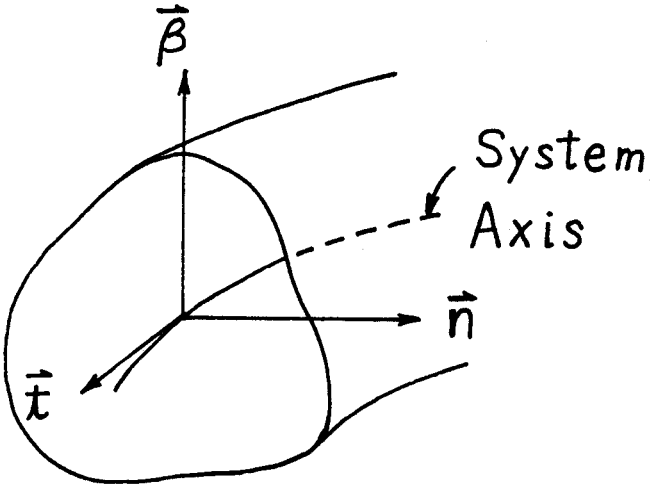
$\vec{\beta}$
System
Axis
$\vec{n}$
$\vec{t}$

Fig. 2

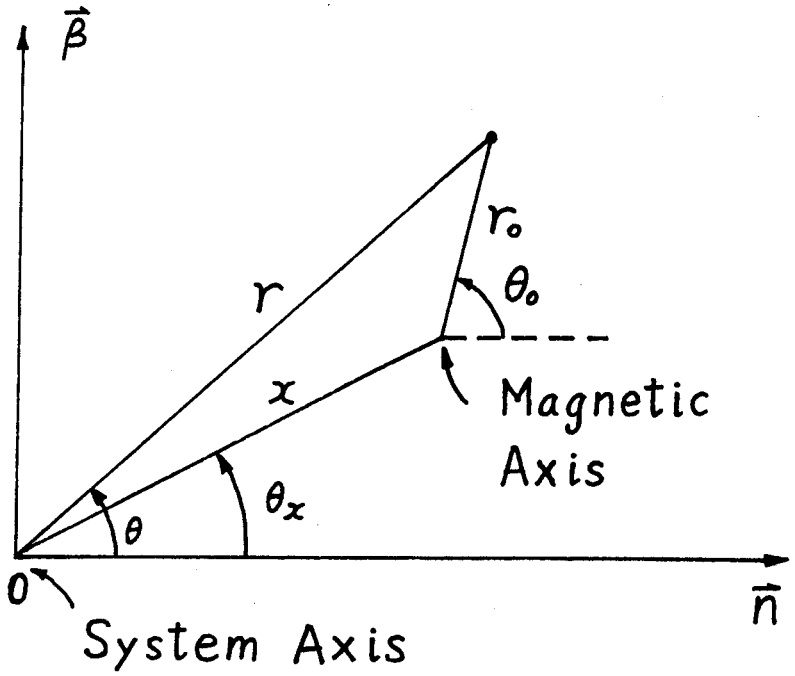
$\vec{\beta}$
r_o
θ_o
r
x
Magnetic
Axis
θ_x
θ
0
$\vec{n}$
System Axis

Fig. 3

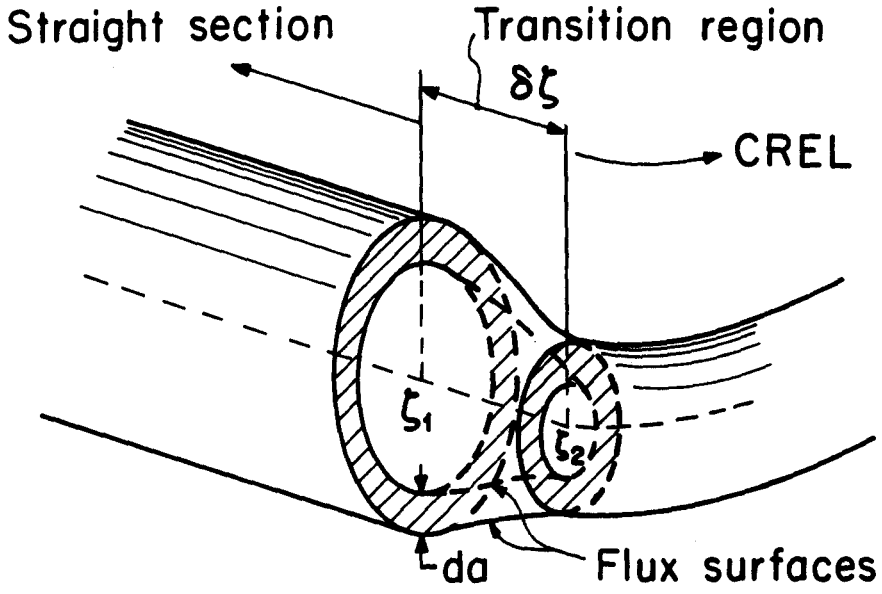
Straight section
Transition region
δζ
CREL
ζ1
ζ2
da
Flux surfaces

Fig. 4

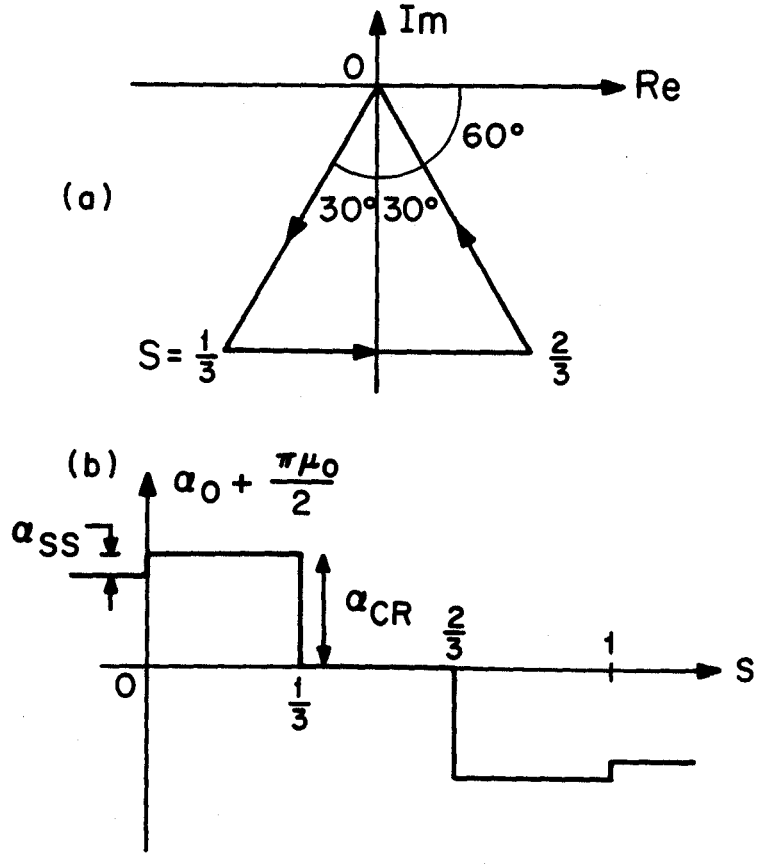
Im
0
Re
60°
(a)
30°
30°
S= 1/3
2/3
(b)
α0 + πμ0/2
αSS
αCR
2/3
1
S
0
1/3

Fig. 5

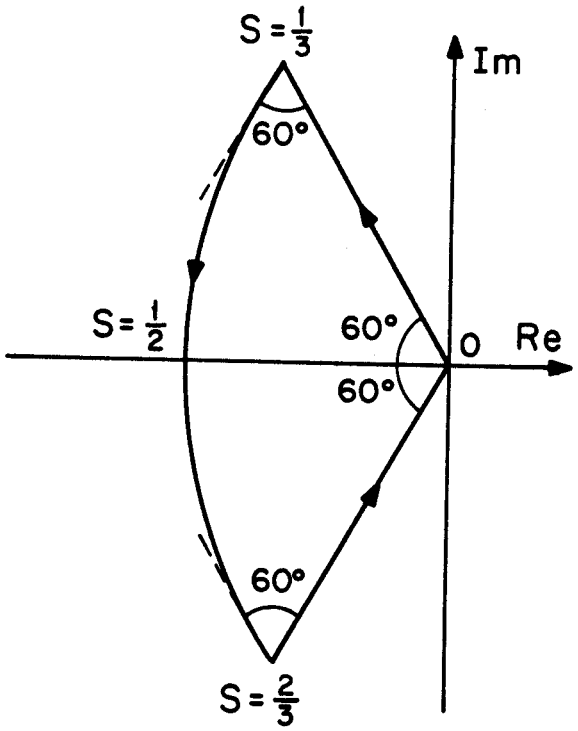

Fig. 6

Fig. 7

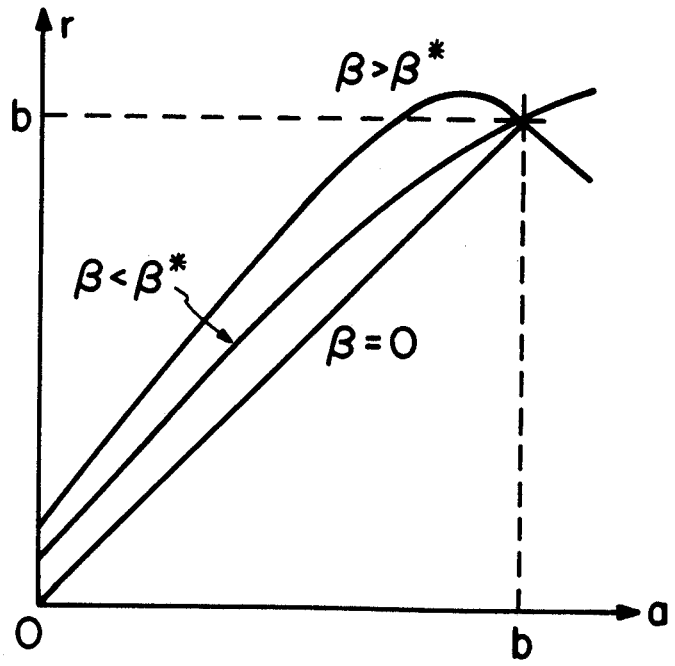

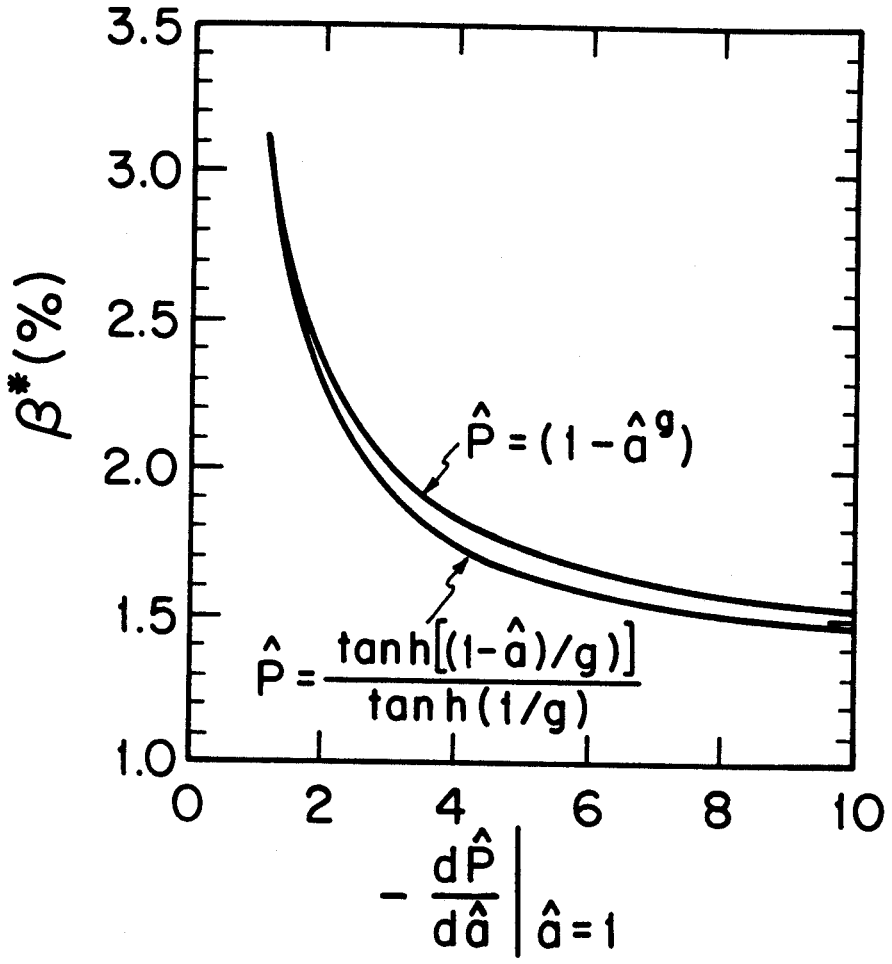
3.5
3.0
2.5
2.0
1.5
1.0
β*(%)
0
2
4
6
8
10
$\hat{P} = (1 - \hat{a}^g)$
$\hat{P} = \frac{\tanh[(1-\hat{a})/g)]}{\tanh(1/g)}$
$-\left.\frac{d\hat{P}}{d\hat{a}}\right|_{\hat{a}=1}$

Fig. 8

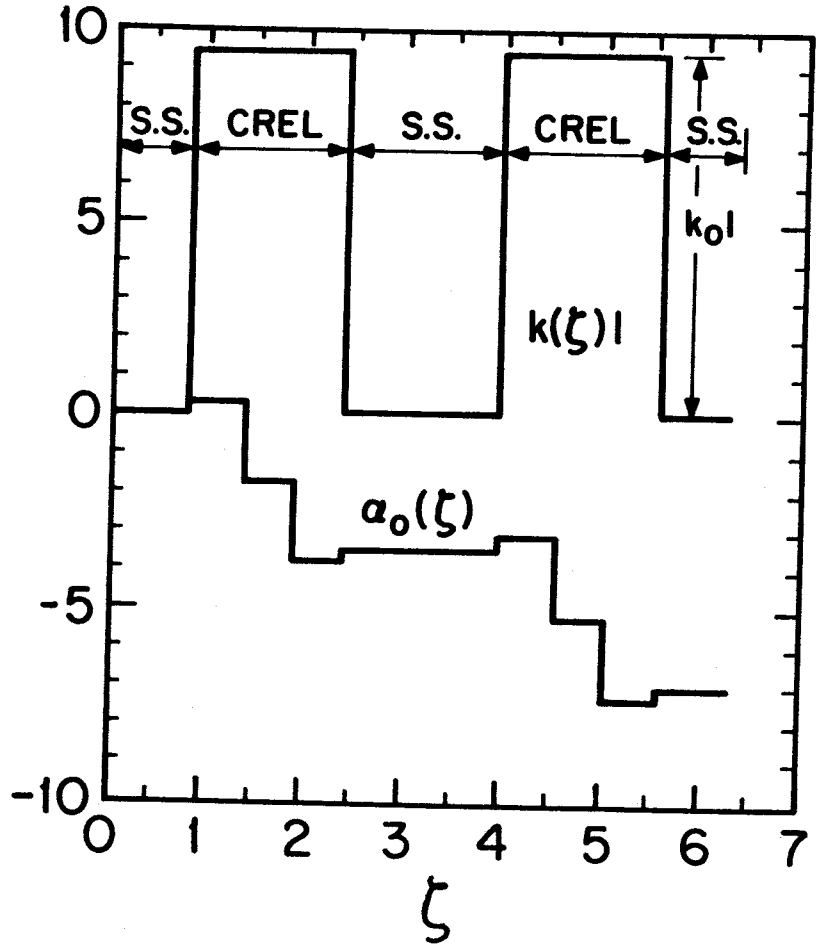
10
5
0
-5
-10
0
1
2
3
4
5
6
7
ζ
S.S.
CREL
S.S.
CREL
S.S.
k₀l
k(ζ)l
a₀(ζ)

(a)

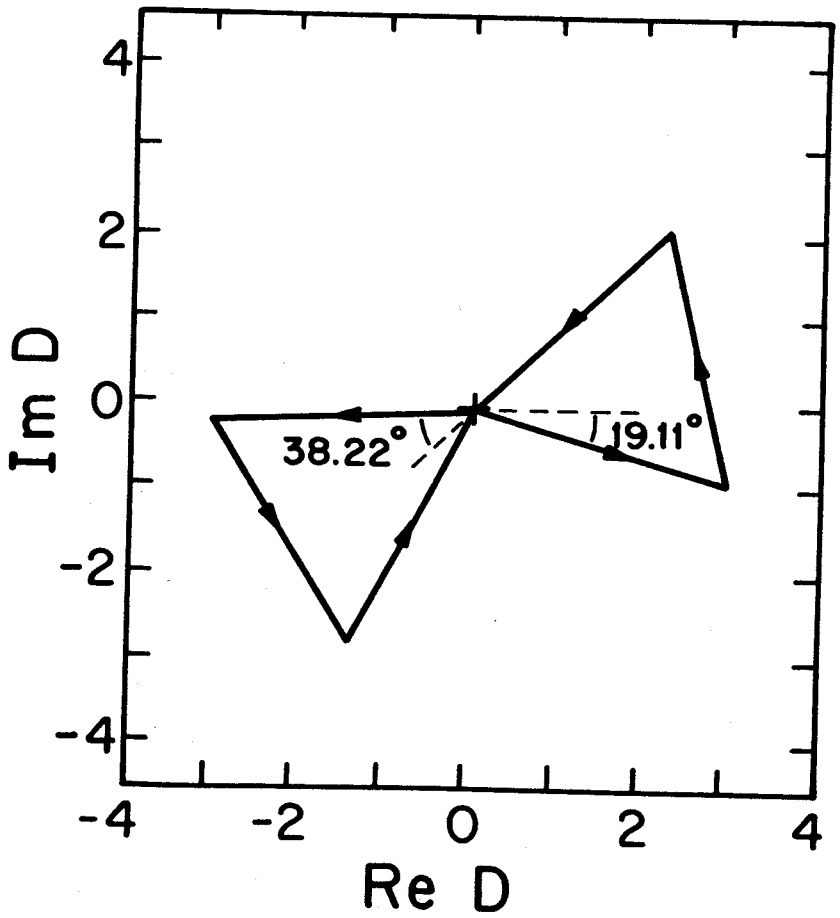
4
2
0
-2
-4
-4
-2
0
2
4
Im D
Re D
38.22°
19.11°

(b)

Fig. 9

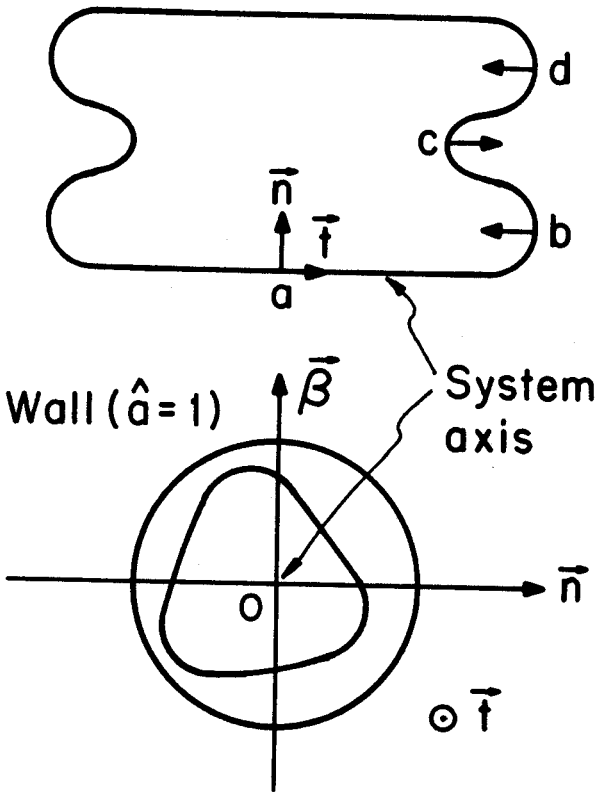
d
c
b
a
$\vec{n}$
$\vec{t}$
Wall ($\hat{a}$ = 1)
$\vec{\beta}$
System
axis
O
$\vec{n}$
$\odot \vec{t}$

Fig. 10

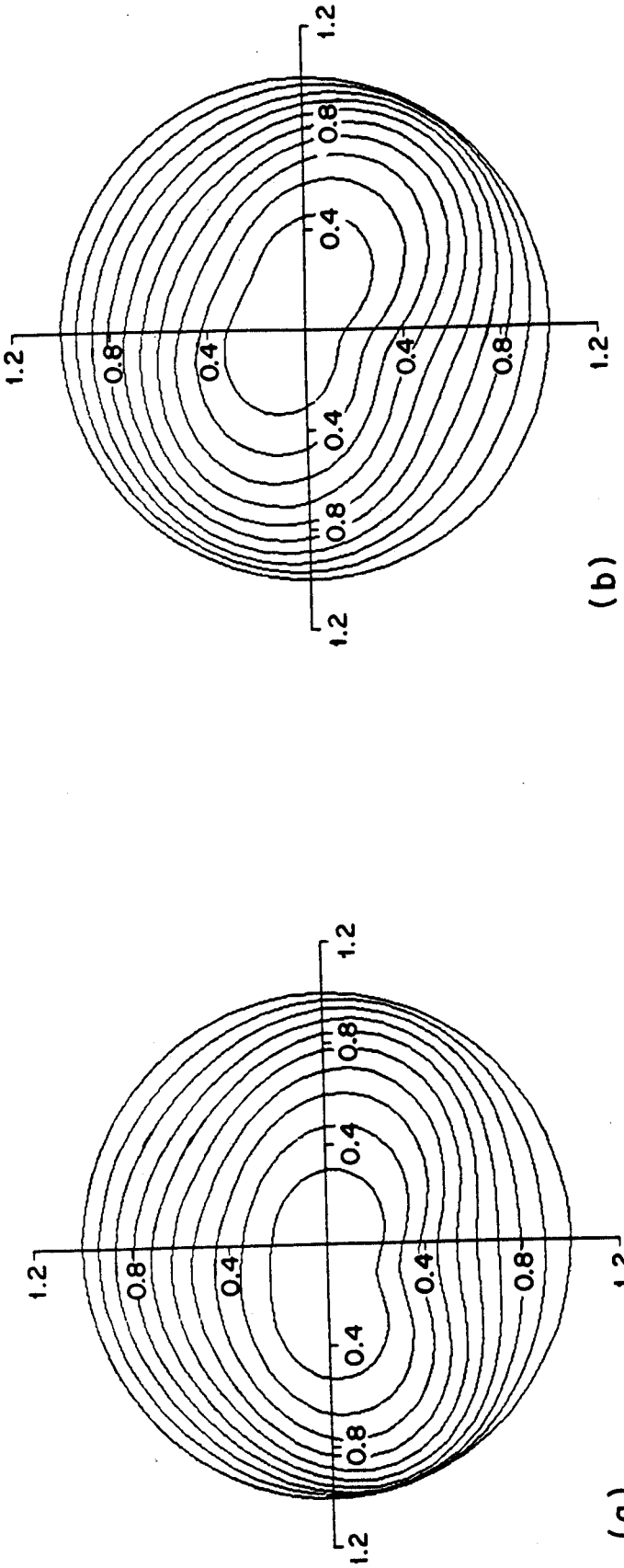

Fig. 11

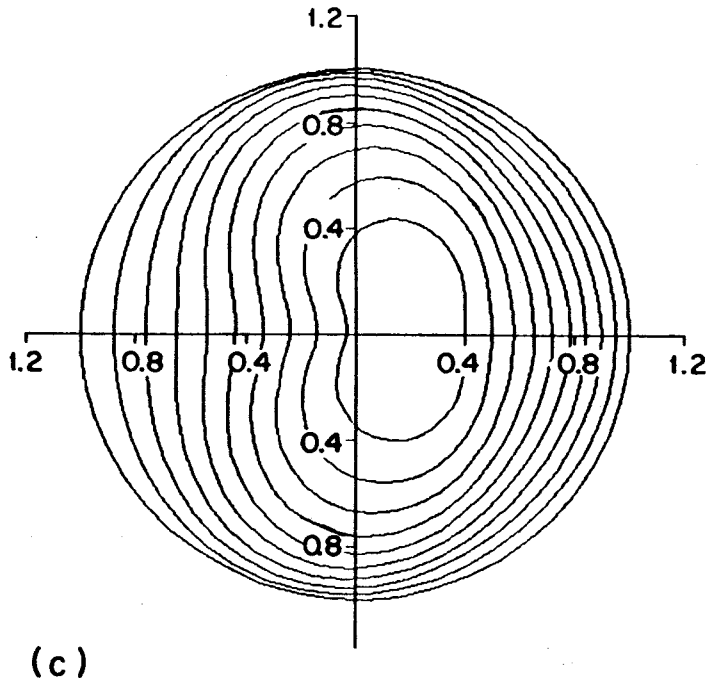

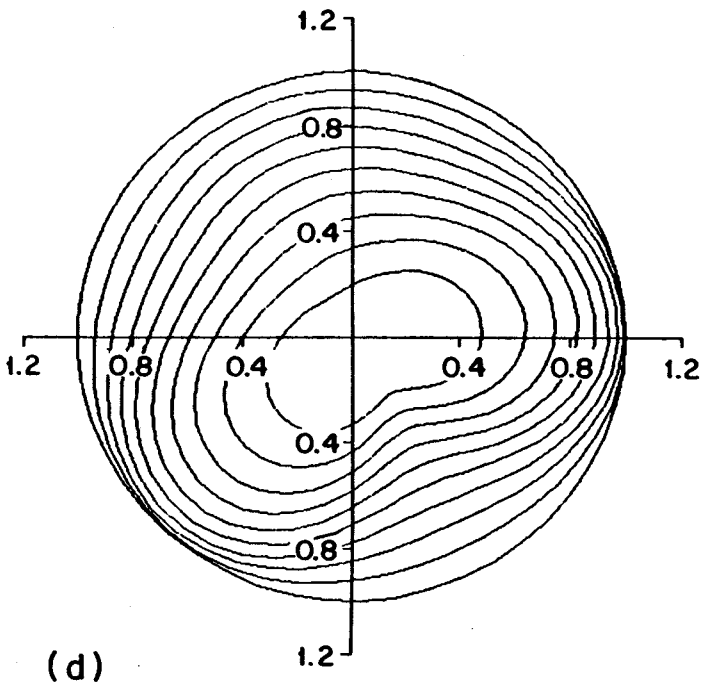

Fig. 11

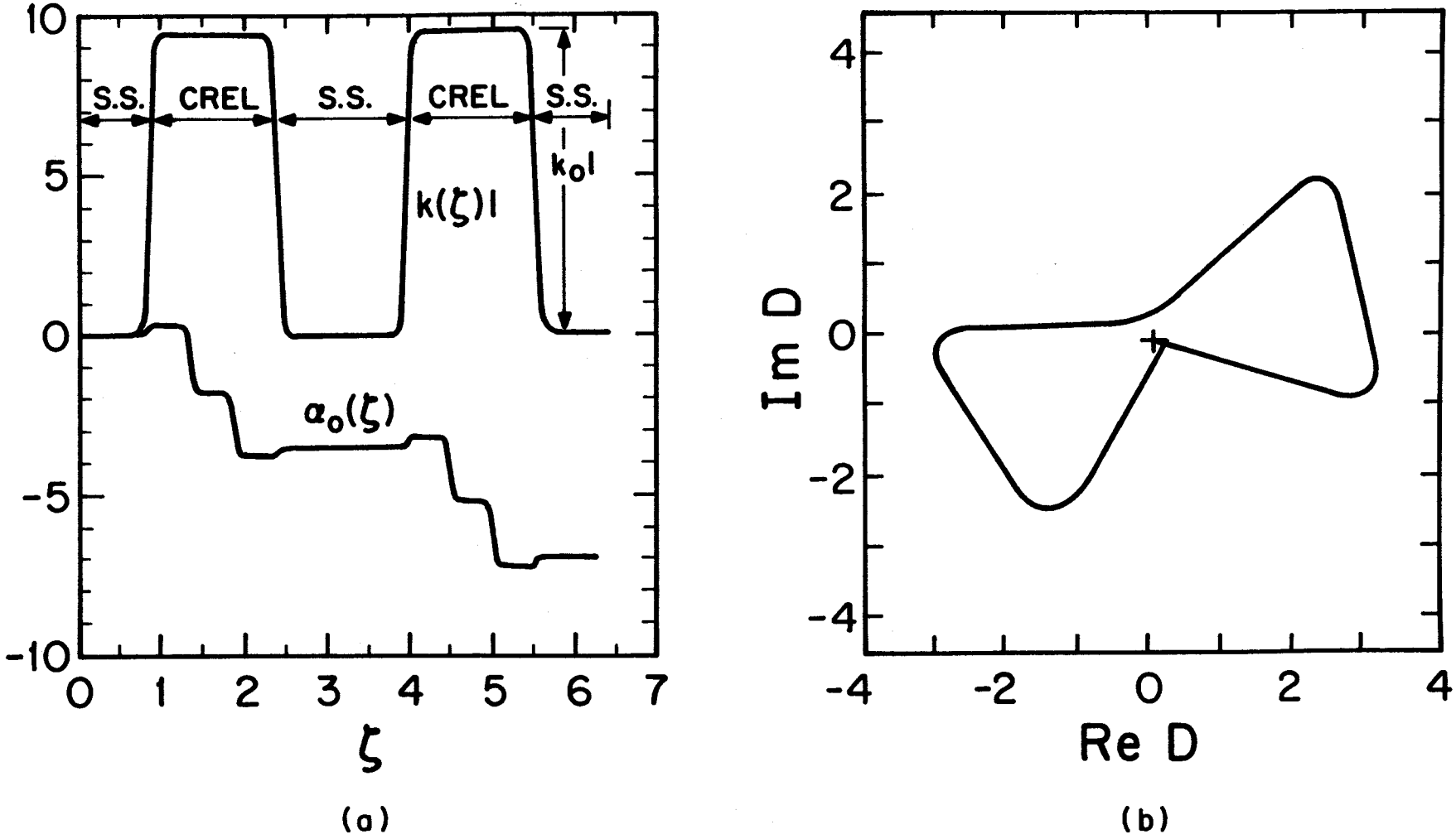
10
5
0
-5
-10
0
1
2
3
4
5
6
7
ζ
S.S.
CREL
S.S.
CREL
S.S.
k(ζ)l
k₀l
α₀(ζ)
(a)
Im D
Re D
4
2
0
-2
-4
-4
-2
0
2
4
(b)

Fig. 12

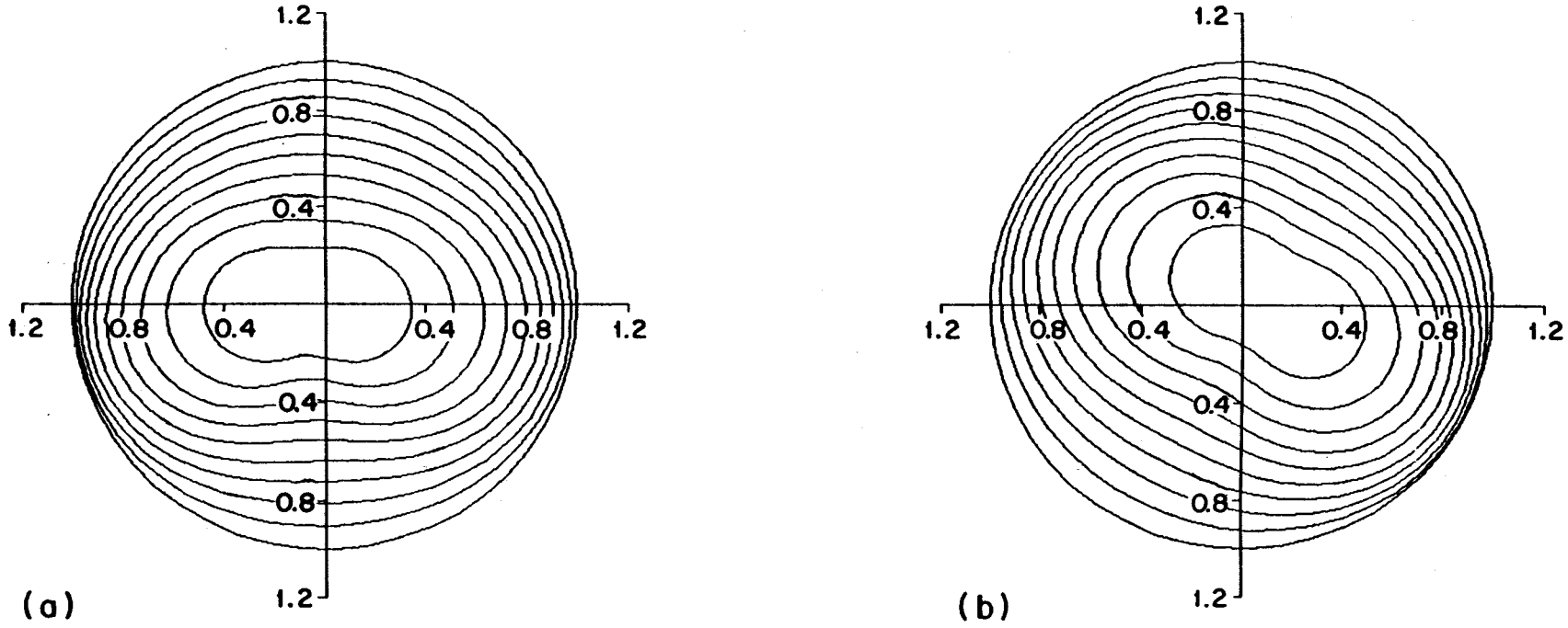
1.2
0.8
0.4
1.2
0.8
0.4
0.4
0.8
1.2
0.4
0.8
1.2
(a)
1.2
0.8
0.4
1.2
0.8
0.4
0.4
0.8
1.2
0.4
0.8
1.2
(b)

Fig. 13

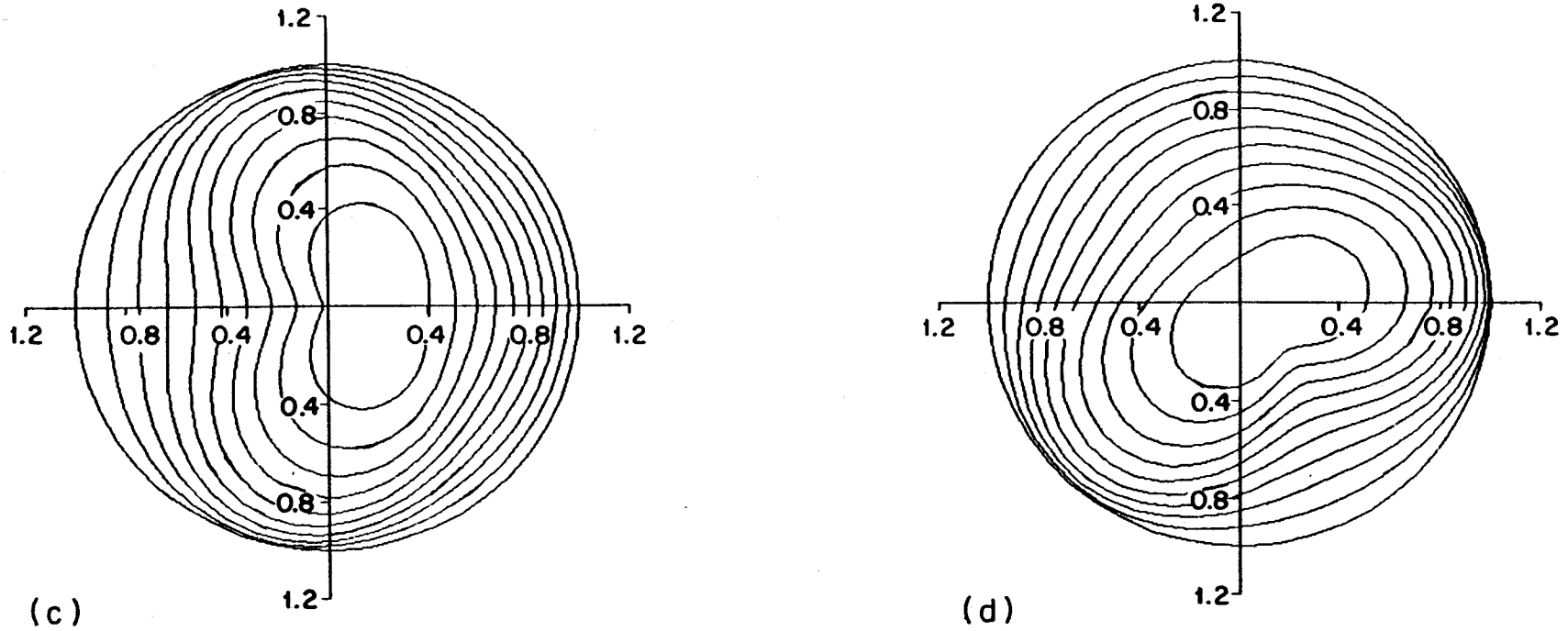
1.2
0.8
0.4
0.4
0.8
1.2
1.2
0.8
0.4
0.4
0.8
1.2
(c)
1.2
0.8
0.4
0.4
0.8
1.2
1.2
0.8
0.4
0.4
0.8
1.2
(d)

Fig. 13

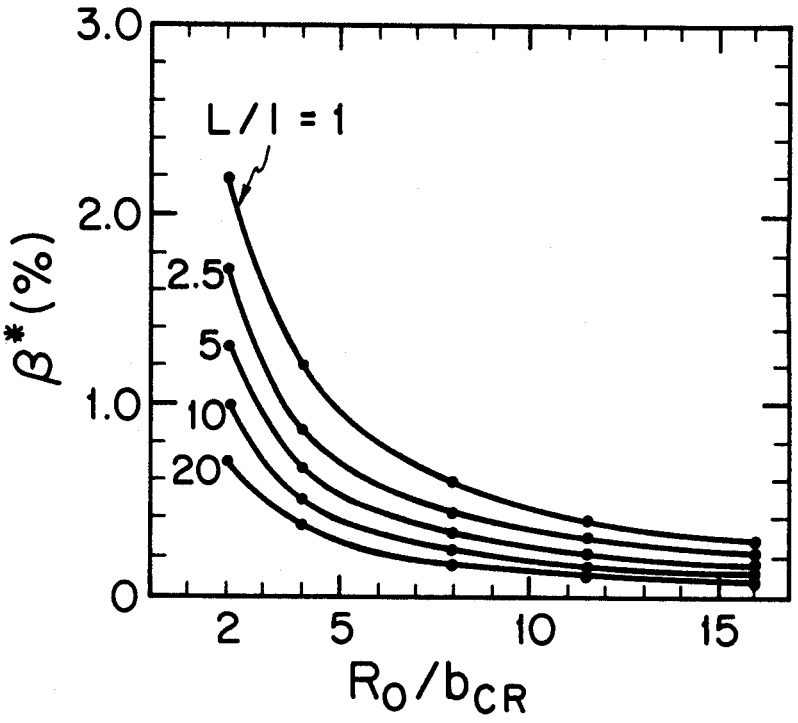

Fig. 14

Fig. 15